Fine-scale topography of the D'' discontinuity and its correlation to volumetric velocity fluctuations

Nozomu Takeuchi [a,*], Kazushige Obara [a,b]

[a] *Earthquake Research Institute, University of Tokyo, Yayoi 1-1-1, Bunkyo-ku, Tokyo 113-0032, Japan*
[b] *National Research Institute for Earth Science and Disaster Prevention, Tsukuba 305-0006, Japan*

ARTICLE INFO

ABSTRACT

We constrained the correlation of the topography of the D'' discontinuity to volumetric velocity fluctuations. We used data obtained from Hi-net tiltmeters deployed by the National Research Institute for Earth Science and Disaster Prevention, Japan, and conducted stacking and migration to map the discontinuity beneath the southwestern Pacific. We compared the obtained map with the distribution of ScS–S travel time residuals, an index of volumetric velocity fluctuations in the lowermost mantle. We detected the fine-scale (of the order of a few hundred kilometers) topography of the D'' discontinuity as well as fine-scale volumetric velocity fluctuations. Regions with relatively higher velocities generally have a discontinuity with shallower depths, and those with relatively lower velocities generally have a discontinuity with deeper depths. The scattering plot between the observed depths of the discontinuity and the observed ScS–S residuals appears to exhibit a nonlinear trend. These results may suggest the existence of both thermal and chemical anomalies, such as those seen in thermochemical plumes.

1. Introduction

Constraining the correlations among various seismological structural parameters provides important clues about the thermal and chemical structures. For example, regions with a deeper 660-km discontinuity appear to correlate well to regions with higher velocities in the transition zone (e.g., Shearer and Masters, 1992; Flanagan and Shearer, 1998), a finding that led to considerable progress in constraining the nature of phase changes and mantle dynamics. In this study, we constrained the fine-scale (of the order of a few hundred kilometers) topography of the D'' discontinuity and its correlation to the volumetric velocity fluctuations in the lowermost mantle.

Because dense seismograph arrays have been installed in several regions, it is now possible to detect the fine-scale topographies of the D'' discontinuity. Previously studied regions include those beneath the Cocos Plate (e.g., Thomas et al., 2004a; Lay et al., 2004; Hutko et al., 2006; Kito et al., 2007), northern Siberia (e.g., Thomas et al., 2004b), the central Pacific (e.g., Lay et al., 2006; Avants et al.,

2006), and the southwestern Pacific (e.g., Yamada and Nakanishi, 1998; Kito et al., 2004). In this study, we focus on the region beneath the southwestern Pacific because the detailed topographies of this region are still controversial.

The structures of the lowermost mantle in this region were mostly constrained from data obtained from a network in Japan. From the time of earlier studies (e.g., Garnero et al., 1993; Shibutani et al., 1993; Shibutani et al., 1995) the D'' discontinuity in this region has been suggested to have a fine-scale topography. Using relatively larger amount of data, Yamada and Nakanishi (1998) and Kito et al. (2004) mapped the lateral fluctuations of the depths. Yamada and Nakanishi (1998) analyzed short-period data from three regional networks in Japan. Kito et al. (2004) analyzed short-period data from two nationwide networks in Japan: J-Array (J-Array Group, 1993) deployed by universities and the Japan Meteorological Agency and Hi-net (Okada, 2004; Obara et al., 2005) deployed by the National Research Institute for Earth Science and Disaster Prevention, Japan. The sampling regions of the data sets used in these studies almost overlap each other. Nonetheless, Yamada and Nakanishi (1998) suggested a deeper discontinuity (170 km from the CMB) in the northeastern region and a shallower discontinuity (270 km from the CMB) in the southwestern region, whereas the P results

---

* Corresponding author. Tel.: +81 3 5841 8497; fax: +81 3 3812 9417.
E-mail address: takeuchi@eri.u-tokyo.ac.jp (N. Takeuchi).

obtained by Kito et al. (2004) suggested a shallower discontinuity (370 km from the CMB) and a deeper discontinuity (240 km from the CMB) in these respective regions. Furthermore, Yamada and Nakanishi (1998) suggested positive *P*-velocity jumps whereas Kito et al. (2004) suggested negative ones. These results indicate that the details of the topography have not yet been conclusively determined.

Recently, several studies (e.g., Tono et al., 2005; Tonegawa et al., 2006, 2008, 2009; Nishida et al., 2008a,b; Kawai et al., 2009) used Hi-net tiltmeters as broadband seismic sensors to retrieve information about the deep interior of the Earth. The advantages of using Hi-net tiltmeters are their high data quality and station density. All such tiltmeter sensors are installed in boreholes, and this is ideal for achieving higher signal-to-noise ratios. Approximately 700 tiltmeters are installed in Japan, and the station density (approximately 30-km spacing) far exceeds that of, for example, USArray (approximately 100-km spacing; http://www.earthscope.org/observatories/usarray). The Hi-net tiltmeters thus provide useful broadband data with unprecedented density.

We stacked and migrated these data to map the topography of the *D″* discontinuity. Note that we retrieved *S* structures by using broadband data, whereas most previous studies retrieved *P* structures by using short-period data. Because the signals of the *D″* discontinuity are generally larger in *S* waves than in *P* waves, it is important to obtain images by using *S* waves. The resultant images were compared with the distribution of *ScS–S* travel time residuals; these are considered to be an index of volumetric velocity fluctuations.

2. Data set

Fig. 1 shows the geometry of the stations and events used in this study. The studied region lies beneath the southwestern Pacific and is located within the Pacific Large Low Shear Velocity Province of, for example, the SH18CE model (Takeuchi, 2007). We used the transverse component of the the Hi-net tiltmeter data. The distance range analyzed was 66.3–76.2°. Tiltmeters have a flat response for ground accelerations. To utilize the broadband features of the waveforms, we weighed longer-period components by integrating the observed seismograms. The resultant seismograms are velocity seismograms. Because longer-period components are predominant in *S* waves, the use of broadband data is advantageous for constraining *S* structures.

Fig. 2 shows an example of the seismograms recorded using the Hi-net tiltmeter and short-period sensors. These are installed at the same location. In the tiltmeter waveforms, we can clearly confirm *ScS* wave packets. This allows us to map the discontinuity by using two different reference phases (*S* and *ScS*). By choosing a better reference phase, we will be able to obtain better models. Note that previous studies used direct *P* or *S* waves as a reference phase (Yamada and Nakanishi, 1998; Kito et al., 2004) due to difficulties in identifying *PcP* or *ScS* in individual traces.

Our data set consists of data from three deep events, as listed in Table 1. We used traces with higher data quality, and the resultant number of traces used were 592, 568, and 456 traces for Events #1, #2, and #3, respectively.

3. Mapping travel time residuals

Before mapping the topography of the discontinuity, we mapped the *ScS–S* travel time residuals. The travel times were measured by using cross-correlation techniques. We first applied a band-pass filter with corner frequencies of 0.01–0.3 Hz to remove higher- and lower-frequency noises. We defined the *S* and *ScS* time
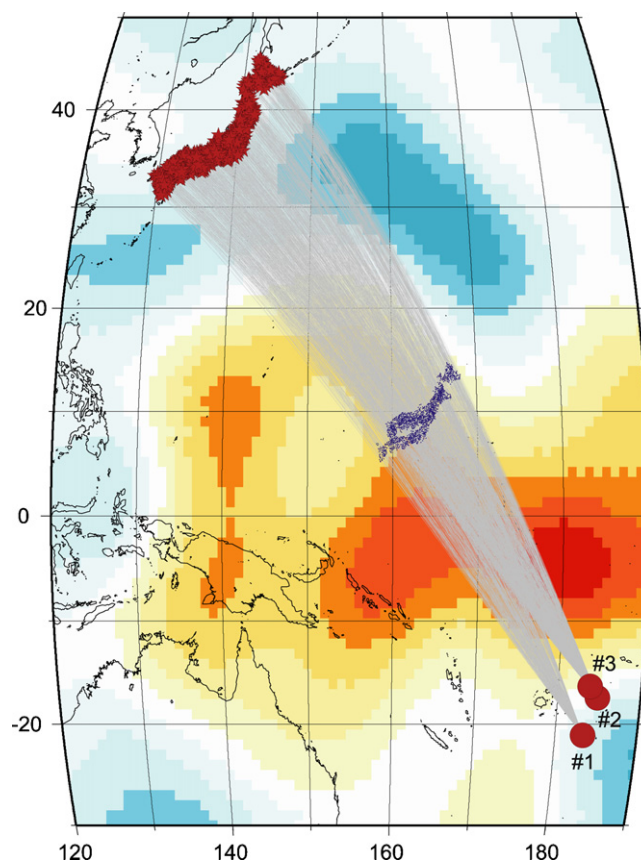

Fig. 1. The geometry of the event-station pairs used in this study. The sources and the stations are indicated by red circles and stars, respectively. The ray paths and the *ScS* bouncing points are indicated by gray lines and blue stars. The heterogeneity patterns at the CMB of the SH18CE model (Takeuchi, 2007) are overplotted.

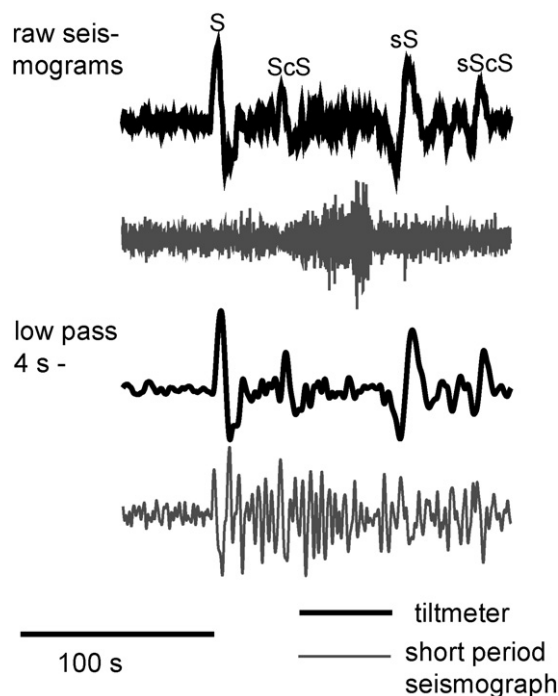**Fig. 2.** Comparison of observed seismograms recorded by a tiltmeter and a short-period sensor at the UNSH station of Hi-net. The records are for Event #1 in Table 1. For comparison, the tiltmeter record is integrated to obtain velocity seismograms. Seismograms obtained without applying a low-pass filter (upper two traces) and those obtained by applying a low-pass filter with a corner period of 4 s (lower two traces) are shown.

Table 1
List of events and source parameters used in this study.

No.	Year	MO	DA	Origin time	LAT	LON	Depth	Mw
#1	2003	07	27	020411.53	−21.08	−176.59	212	6.6
#2	2003	03	14	125412.12	−17.42	−175.18	274	6.4
#3	2002	08	09	133105.29	−16.31	−176.17	364	6.1

windows by extracting the data between −5 and 10 s from the observed peak of the main pulse.

We first show the distributions of the observed travel time residuals projected at the stations (Fig. 3). To enhance variations within the array, we plot deviations from the averaged residuals for each event (5.99 s, 5.90 s, and 5.97 s for Events #1, #2, and #3, respectively). The travel time residuals were computed with respect to the synthetic travel times computed for the IASP91 model (Kennett and Engdahl, 1991). Almost all of the observed residuals are positive, suggesting that all of the studied regions are located within the low-velocity province beneath the Pacific (e.g., Mégnin and Romanowicz, 2000; Gu et al., 2001; Takeuchi, 2007). The results shown in Fig. 3 indicate that the apparent distribution of residuals is event-dependent. Positive residuals are observed at stations in the central part of Japan for Event #1, whereas they are observed at stations in the western part of Japan for Events #2 and #3. This suggests that the observed residuals are not primarily due to heterogeneities in the vicinity of stations.

Next, we show the distribution of the residuals projected at the bouncing points of ScS (Fig. 4). We show the deviations from the averaged residuals for all of the data (5.95 s). It can be seen that the bouncing points plotted by red stars are confined to a small area (approximately 4° × 4° large). The amount of fluctuations of the residuals reaches to approximately 8 s (as shown in Fig. 5a), and such large fluctuations are difficult to explain by event mislocations or the topography of the D'' discontinuity. Therefore, these results suggest that these residuals are primarily due to volumetric heterogeneities in the lowermost mantle. We thus use the resultant distribution of the residuals as an index of the volumetric velocity fluctuations in the lowermost mantle.

Fig. 4 intuitively shows the existence of fine-scale (of the order of a few hundred kilometers) heterogeneities of the volumetric velocity fluctuations. Hereafter, we mainly focus on depth variations of the D'' discontinuity as a function of ScS–S residuals (plotted in

Fig. 4. ScS–S travel time residuals projected at the ScS bouncing points. All data for Events #1–#3 are combined. We plotted deviations from the average of the plotted data (5.95 s).

Fig. 4). Therefore, we used the results shown in Fig. 4 for defining data bins.

4. Mapping D'' discontinuity

4.1. Definition of data bins

We define data bins and stack and migrate each data bin in order to locate the D'' discontinuity. Fig. 5a shows the observed ScS–S residuals plotted as a function of the azimuth, which is defined by the direction from the centroid of the epicenters of Events #1–#3 to each bouncing point of ScS. The residuals are primarily a function of the azimuth only with a slight dependence on events and epicentral distances. The results suggest the plausibility of considering only the azimuthal heterogeneities, at least, in the studied region. In the discussions below, we therefore use the azimuth as an index to specify the locations.

We defined data bins by using this index. We categorized traces whose azimuth is − 316, 316–321, 321–325, 325–329, and 330 – as data bins #1, #2, #3, #4, and #5, respectively. The number of traces belonging to each data bin is 232, 571, 358, 289, and 166, respectively. Fig. 5b shows the comparison between the spatial scales of the data bins and the typical Fresnel zone. We defined relatively smaller bins to suppress the fluctuations of SdS–S or ScS–SdS residuals within each bin; this should improve the coherency of the SdS signals.
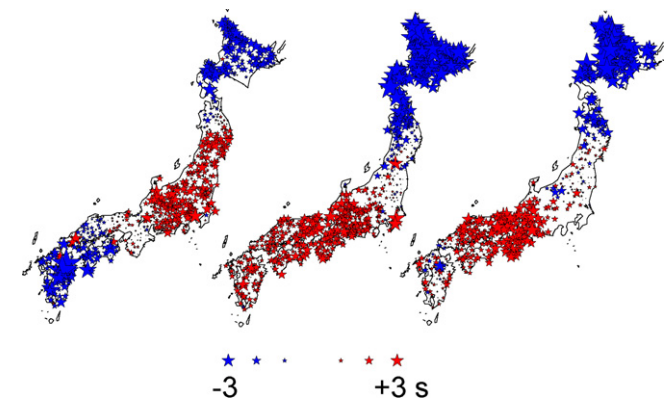

Fig. 3. ScS–S travel time residuals projected at the stations. Residuals for Events #1 (left), #2 (center), and #3 (right) are plotted. Deviations from the averaged residuals (5.99 s, 5.90 s, and 5.97 s for Events #1, #2, and #3, respectively) are plotted. Red and blue stars indicate positive and negative residuals, respectively, and the size of the symbols indicates the absolute value of the residual.
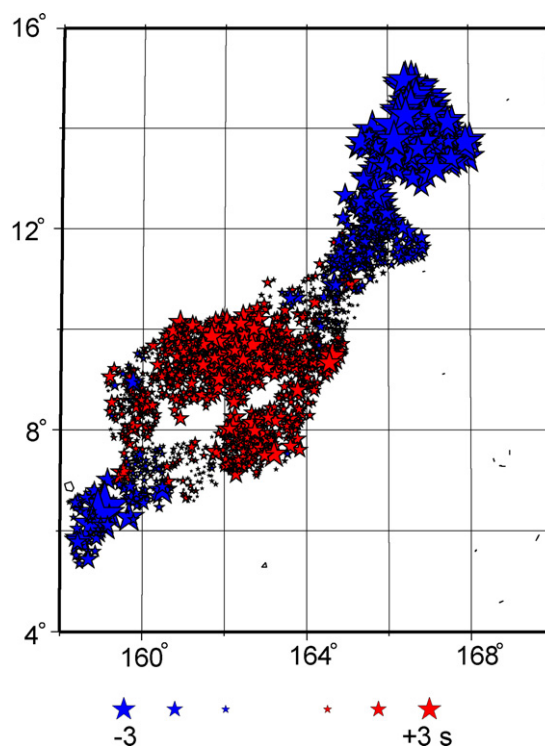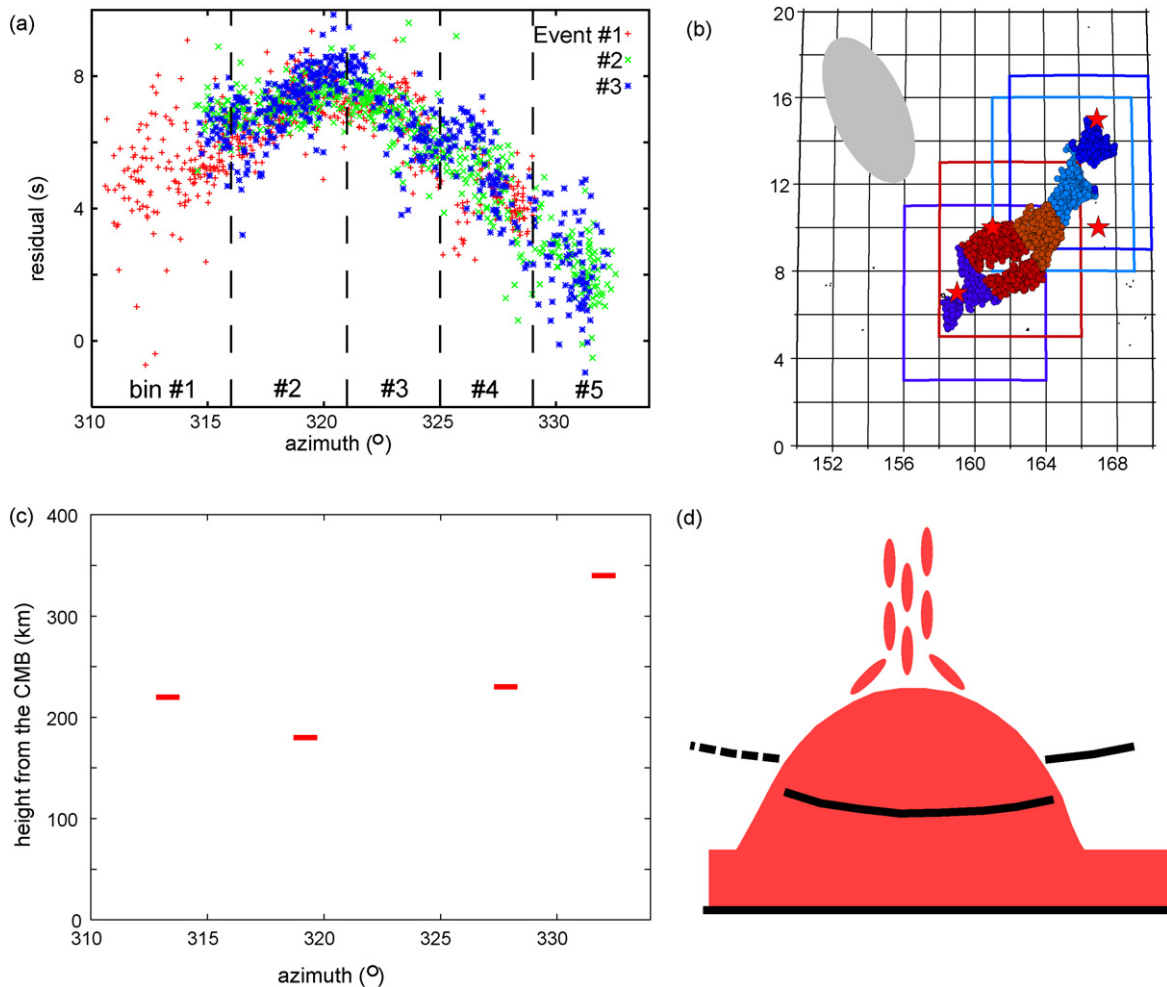
Fig. 5. (a) The observed *ScS–S* residuals for Events #1 (red), #2 (green), and #3 (blue) as a function of the azimuth of the *ScS* bouncing point. The vertical dashed lines indicate the boundary of data bins #1–#5 defined in this study. See the text for the definitions of the azimuth and the data bins. (b) The distributions of the *ScS* bounding points belonging to each data bin. Circles filled with the same color indicate the data belonging to the same bin. For comparison, the typical size of the Fresnel zone (gray ellipse in the upper left) is plotted. Colored squares indicate the regions used to present the results of the migrations shown in Fig. 9, and the red stars indicate the locations of the imaged scattering sources. (c) The azimuth and the depth of the scattering sources imaged by the migrations shown in Fig. 9. (d) A schematic picture explaining the trends observed in (a) and (c). The regions colored in red indicate the chemically distinct regions. The black lines indicate the discontinuities. The discontinuity that could not be constrained by the data set in this study is indicated by the broken line.

4.2. Results by stacking

We first conducted double-array stacking to detect the *SdS* signals. Because the array has a large aperture, we used the method by Yamada and Nakanishi (1996) rather than that by Krüger et al. (1993). Although signals can be confirmed even by linear stacks, we conducted 2nd root stacks (Kanasewich, 1973) to further enhance the signals. We conducted two types of stacking: stacking using *ScS* as a reference phase and stacking using *S* as a reference phase. We can reduce the uncertainties due to lateral heterogeneities by choosing a better reference phase.

The stacking method is essentially the same as that by Yamada and Nakanishi (1996). After applying a band-pass filter with corner frequencies of 0.01–0.3 Hz, we shifted the times of each trace so that the observed travel times of the reference phase (*ScS* or *S*) are equal to zero. The observed *S* travel times are defined by the peak time of the *S* packet, and the observed *ScS* travel times are defined by adding the measured *ScS–S* travel time (shown in Fig. 4) to the observed *S* travel time. We normalized each trace so that the peak amplitudes of *S* were equal to unity. The stacked waveform *y* for the assumed discontinuity depth *d* at time *t*

is then computed by:

$$y(t, d) = R(t, d)|R(t, d)|, \qquad (1)$$

where

$$R(t, d)$$

$$= \frac{1}{N} \sum_{j=1}^{N} sgn[x_j(t + (\tau_j(d) - \tau_1(d)))] \times |x_j(t + (\tau_j(d) - \tau_1(d)))|^{1/2}. \qquad (2)$$

We denote the number of traces as *N*, the observed waveform (after the time shift and normalization) for the *j*th trace as x_j, and the predicted time delay of the *SdS* phase from the assumed discontinuity for the *j*th trace as τ_j. The assumed discontinuity depth, *d*, corresponds to the slowness in the conventional slant stacking. The assumed depth at the peak in the stacked seismograms is not necessarily equal to the actual depth of the discontinuity because it can be biased by lateral heterogeneities. To avoid confusion, we hereafter call this parameter as the "slowness" rather than the "assumed depth."
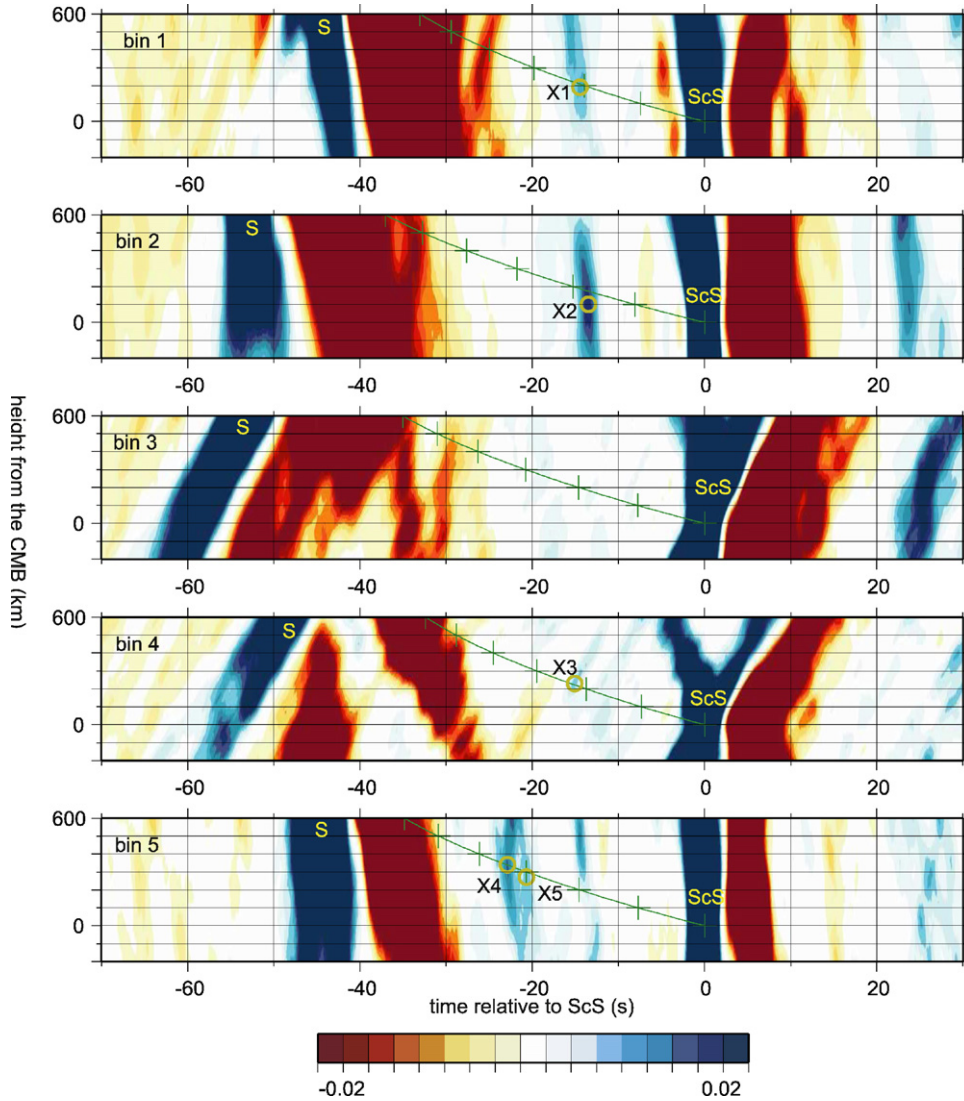
Fig. 6. Results of double-array stacking for data bins #1–#5 when we use *ScS* as a reference phase. Horizontal and vertical axes represents the time relative to the reference phase and the assumed depth of the discontinuity (corresponding to the slowness in conventional slant stacking), respectively. Green lines indicate the predicted slowness-time combinations for reflections from the flat discontinuity. The predicted slowness and time for the discontinuity at 0, 100, 200, . . . , 600 km from the CMB are also plotted by green crosses. Signals for *S* and *ScS* are indicated by yellow texts. The yellow circles indicate the relatively strong peaks discussed in this paper.

Figs. 6 and 7 show the results of stacking for each data bin when the reference phase is *ScS* and *S*, respectively. The green lines denote a theoretical curve of *SdS* locations computed by using the reference model, IASP91. We can identify five relatively strong peaks in the vicinity of the theoretical curve with a maximum amplitude greater than 0.067 (indicated in deep blue), and we labeled the phase associated with each signal as X1–X5, respectively. All of the peaks are positive peaks, suggesting that the *D″* discontinuity in this region is likely to have a positive jump (the lower layer has a higher velocity than the upper layer). Note that we are discussing *S* velocity structures and we cannot directly compare these results with previous *P* results (e.g., Shibutani et al., 1993, 1995; Yamada and Nakanishi, 1998; Kito et al., 2004). Note also that our results are consistent with preliminary *S* results obtained by Garnero et al., 1993; Konishi et al., 2009. The observed peaks shown in Figs. 6 and 7 probably do not clearly exhibit two-sided peaks because the stacked *SdS* signals were not completely in phase.

In Fig. 7, we also plot the peak locations for *ScS*. The peaks deviate from the synthetic locations (right end of the green line) in terms of both time and slowness, suggesting that lateral heterogeneities

have significant effects. The deviations are 2.2–7.2 s in time and 0–160 km in slowness, indicating that the choice of the reference phase is critical.

In this study, we chose *ScS* as the reference phase because the amplitudes of the peaks of the *SdS* signals are more enhanced. The amplitudes of X1–X5 in Fig. 6 are 0.011, 0.019, 0.009, 0.009, and 0.015, respectively, whereas those in Fig. 7 are 0.011, 0.013, 0.007, 0.009, and 0.012, respectively. The measurements of *ScS* arrival times are less accurate as compared to those of *S* arrivals; this will cause incoherency and reduce the amplitudes of the signals in the stacked waveforms. Nonetheless, we see improvements in the amplitudes, suggesting that the use of *ScS* is more appropriate.

However, some of the detected peaks still deviate from the values predicted by the IASP91 model in terms of both the slowness and the incident azimuth. In Fig. 6, we see that the slownesses for X1, X3, and X4 are close to the prediction, whereas those for X2 and X5 are anomalous. X5 is also anomalous in terms of the incident azimuth. In Fig. 8, we show the estimated incident azimuth of each signal. We first rotate the epicenters of Events #1–#3 in
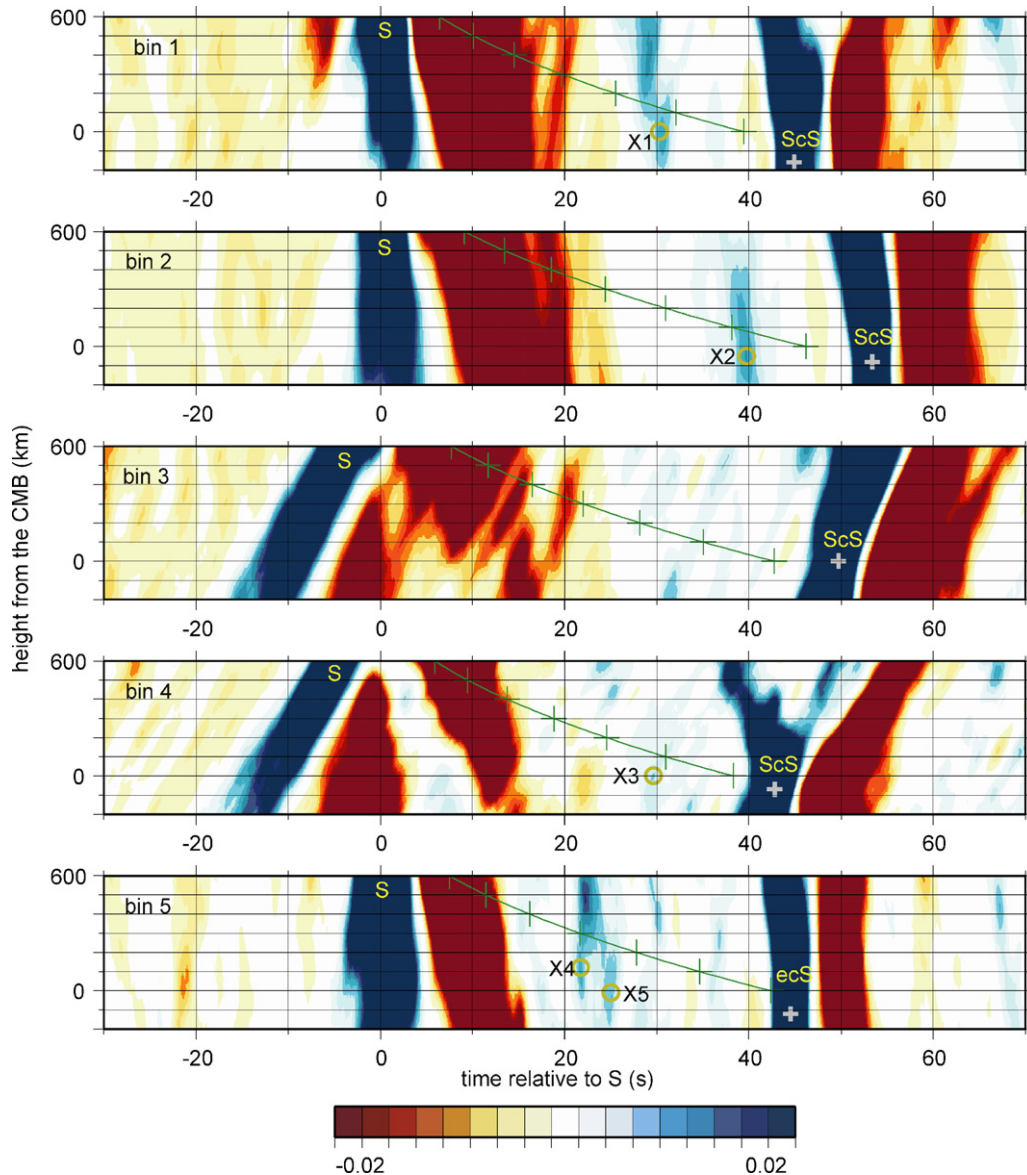
Fig. 7. The same as Fig. 6 except that the reference phase is *S*. The observed peaks for *ScS* are indicated by gray crosses.

the counter-clockwise direction with respect to the pivoting station (the 1st station in Eq. (2)) for the degrees of ϕ. We then stack the seismograms by using Eq. (2). We assume the obtained results to be the stacked seismograms for the relative incident azimuth of ϕ with respect to the great circle plane. Note that if we have a peak of the stacked seismograms in the positive relative azimuth, it suggests that the incident wave is incident from the eastward direction of the great circle plane. The results shown in Fig. 8 suggest that the incident waves for X1–X4 are incident almost from the great circle whereas that for X5 is incident from the westward direction of the great circle.

In summary, the slownesses and the incident azimuths for X1–X4 do not differ considerably from the predicted values, whereas those for X5 are very anomalous. It is notable that the slowness for X5 in Fig. 8e (430 km) differs considerably from that in Fig. 6 (270 km), indicating that the incident angle is also very anomalous. It should be difficult to accurately locate the scattering source for such anomalous signals partly because such complex scattering waves may have complex directivity that cannot be accurately evaluated by the current data set. Therefore, we do not discuss the location of the scattering source for X5.

Comparing the apparent reflection depths of X1–X4, that for X2 appears to be the deepest and that for X4 appears to be the shallowest. When we assume that the discontinuity is flat and Earth's structure in the studied region is close to the lateral homogeneous reference model, we can evaluate the depth of the discontinuity from the observed *ScS–SdS* travel times. The obtained depths for X1–X4 are 210 km, 170 km, 220 km, and 340 km height from the CMB, respectively. We can also evaluate the depths from the observed *SdS* slownesses. The obtained depths are 190 km, 100 km, 230 km, and 340 km height, respectively. Although the general trends of the topography are robust, we see discrepancies between the locations evaluated from the travel times and the slownesses. To locate the depths of the discontinuity more accurately, in the next subsection, we conduct migration without using the assumption of lateral homogeneity.

4.3. Results by migration

We now locate the scattering sources for X1–X4 by migration. By interpolating the imaged sources, we constrain the topography of the D'' discontinuity. We conducted migration by essentially using
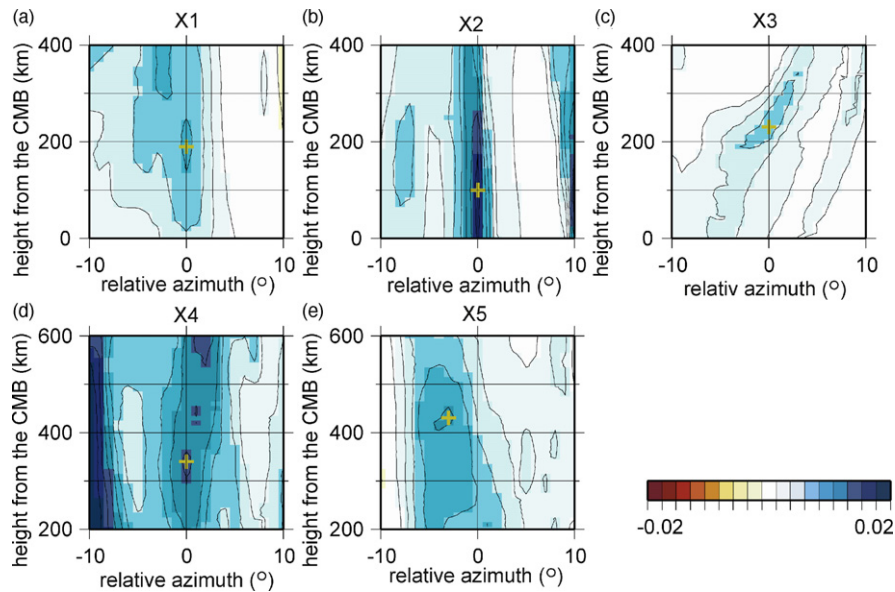
Fig. 8. (a) The stacked seismograms of data bin #1 as a function of the incident azimuth and the assumed depth (slowness) for the peak for X1 in Fig. 6. (b–e) Those of data bins #2, #4, #5, and #5 for X2, X3, X4, and X5, respectively.
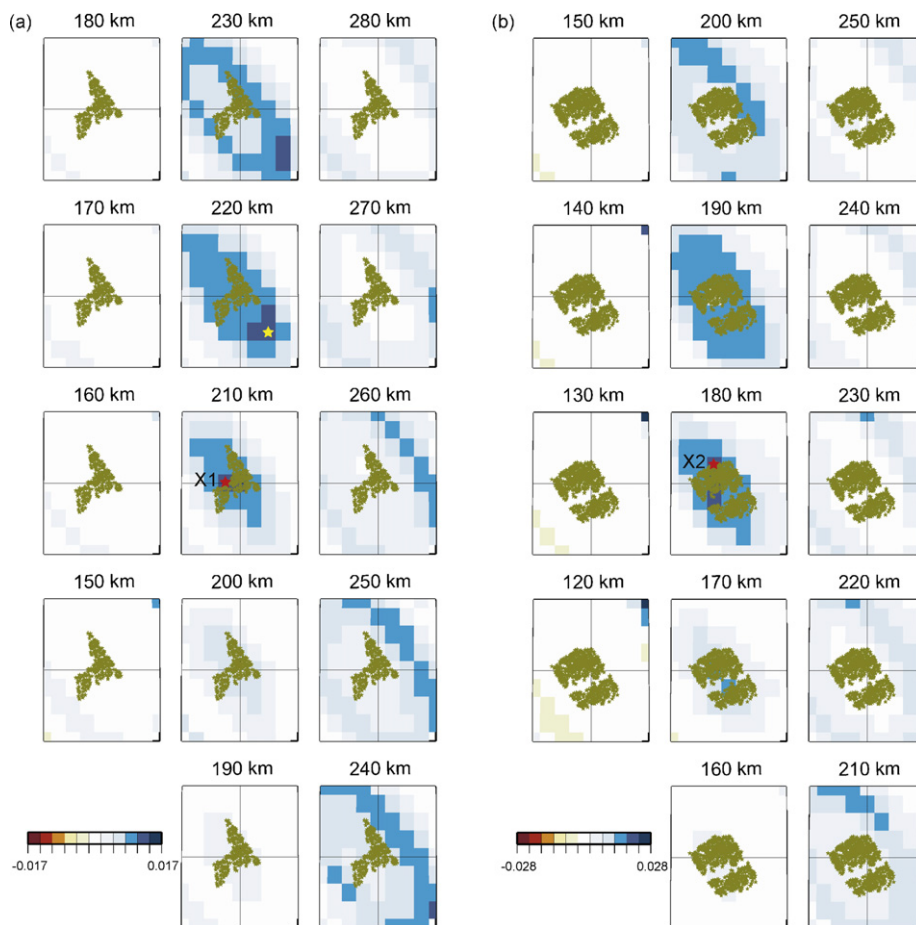

Fig. 9. (a) Results of the migration of data bin #1. The displayed region is between 156–164°E and 3–11° N. The imaged scattering source for X1 is indicated by the red star. Another remarkable local maximum is indicated by the yellow star. For reference, the ray theoretical *ScS* bouncing points are overplotted. (b) Results of data bin #2 and the imaged scattering source for X2. The displayed region is between 158–166°E and 5–11°N. (c) Results of data bin #4 and the imaged scattering source for X3. Another remarkable local maximum is indicated by the yellow star. The displayed region is between 161–169°E and 8–16°N. (d) Results of data bin #5 and the imaged scattering source for X4. The displayed region is between 162E–170°E and 9–17°N.
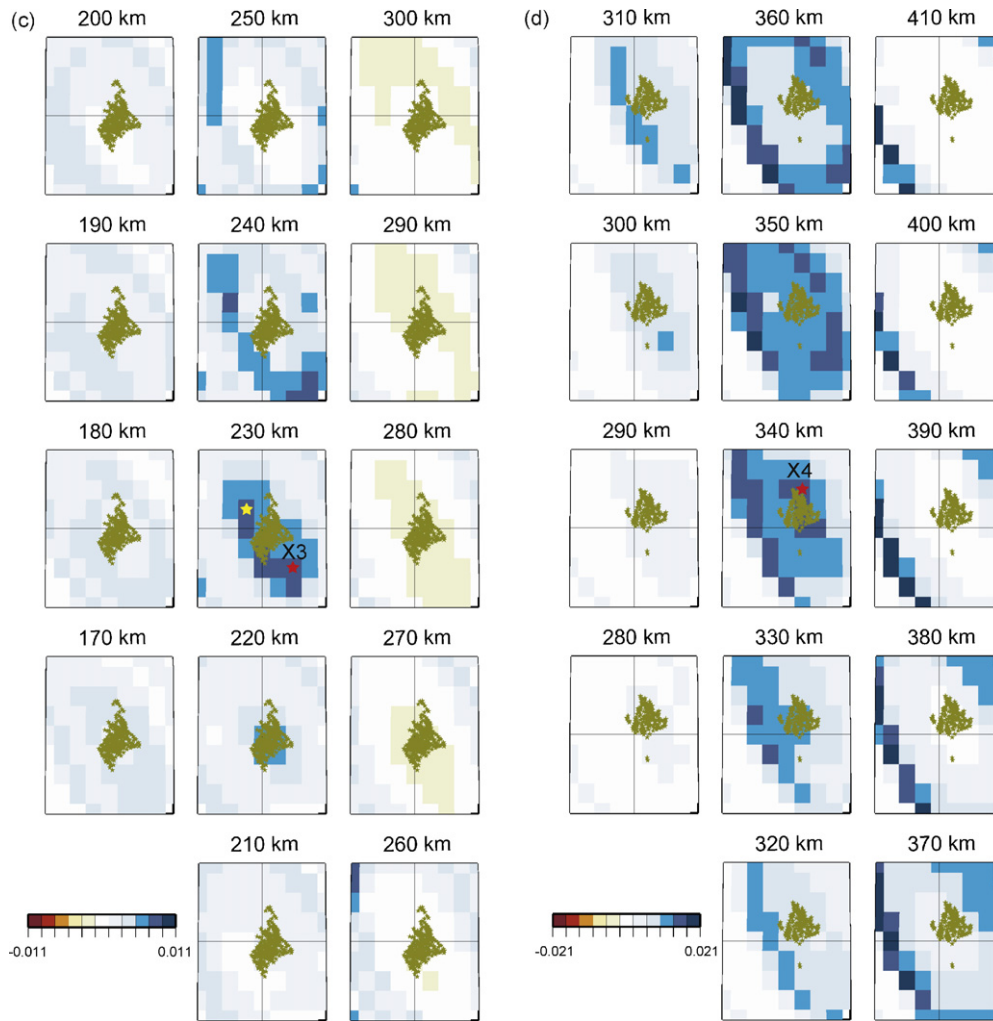
Fig. 9. (*Continued*).

the same method as that used by Thomas et al. (1999, 2004b). Our migration method can be described as follows. The amplitude of the migrated image, *z*, for the *k*th scattering points, q_k, is computed as:

$$z(q_k) = S(q_k)|S(q_k)|, \tag{3}$$

where

$$S(q_k) = \frac{1}{N}\sum_{j=1}^{N}\mathrm{sgn}[x_j(\tau_{jk})]|x_j(\tau_{jk})|^{1/2}. \tag{4}$$

Here, we denote the synthetic arrival time of the scattering wave for the *k*th scattering point and the *j*th station as τ_{jk}. We use the same x_j as those used in Eq. (2). In this migration, we chose *ScS* as the reference phase.

We defined 21×21 scattering points in the horizontal direction with $1° \times 1°$ intervals and 81 scattering points in the vertical direction with 10 km intervals between 0–20°N, 160–180°E, and -200 km and 600 km height from the CMB. The total number of scattering points defined is thus 35,421. The grid intervals are sufficiently small as compared to the typical size of the Fresnel zone (approximately 5° wide, 8° long, and 30-km thick).

Fig. 9 shows the results of our migration. Because of the limitations of space, we plot only the results in the vicinity of the ray

theoretical bouncing points of *ScS* (indicated by boxes in Fig. 5b). In Fig. 9a, the local maximum identified as the source for X1 is observed at the 210 km height from the CMB. We see another local maximum (indicated by a yellow star) at the 220 km depth; this probably corresponds to the peak located at the upper left of X1 in Fig. 6. In Fig. 9b, the local maximum for X2 is imaged at the northern end of the regions of *ScS* bouncing points. The result is consistent with the fact that the slowness of the peak for X2 in Fig. 6 was slightly smaller than the prediction. In Fig. 9c, we see two local maxima at the 230 km height. We may have two scattering sources at this depth or one scattering source at a slightly deeper depth. In either case, because the azimuths of these two scatterers are almost identical, the robust conclusion is that we can locate the source for X3 at approximately 230 km height around this azimuth. In Fig. 9d, we located the source for X4 at the 340 km height. We see additional strong scattering sources in the western part of the displayed region; these are probably scatterers for X5.

The depths and azimuths of the located scattering sources are plotted in Fig. 5c. The results indicate that the azimuths with large positive residuals tend to have a deeper discontinuity whereas those with smaller residuals tend to have a shallower discontinuity. Below, we quantify the correlation between the topography of the discontinuity and the *ScS*–*S* residuals.
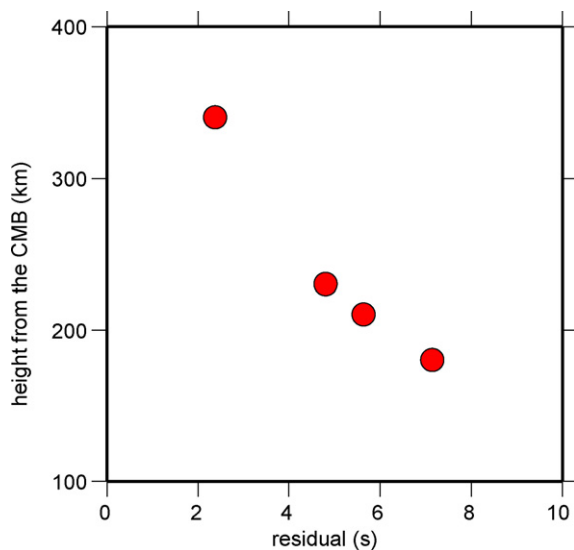
Fig. 10. A scattering plot between the depths of the detected scattering sources (for X1–X4) and the observed *ScS–S* residuals at the azimuth of the detected locations.

5. Discussion and conclusion

We detected fine-scale heterogeneities in volumetric velocity fluctuations (Fig. 5a). The *ScS–S* residuals fluctuate between approximately 0–8 s. The 8 s residual corresponds to 3% velocity reductions in the lowermost 500 km. We also detected the fine-scale topography of the D'' discontinuity (Fig. 5c). We found that they are correlated with each other: there exist general trends of shallower depths of the discontinuity in regions with relatively higher velocities and vice versa in regions with lower velocities.

The observed topography is not likely due to an artifact by the volumetric velocity fluctuations. If we have volumetric lower-velocity anomalies, the observed *ScS–SdS* will be larger than the prediction, causing an apparently shallower discontinuity. Nonetheless, we observed a deeper discontinuity at the lower-velocity regions (Fig. 5a and c), suggesting the robustness of the observed trend.

To quantify the correlations between the topography and the volumetric heterogeneities, we obtained a scattering plot between the depths of the detected scattering sources and the *ScS–S* residuals (Fig. 10). The *ScS–S* residuals are evaluated by averaging the observed data whose azimuth is within $\pm 1°$ from the azimuth of the located scattering sources. The source for the smallest residuals (the source for X4) is located at an anomalously shallower depth, and the correlations in Fig. 10 appear to exhibit a nonlinear trend.

If we assume that the D'' discontinuity is caused by a phase change, the topography of the discontinuity can be assumed to be an index for the pressure perturbations, dP, of the phase boundary. If we assume that the thickness of the low-velocity province is invariant in the studied region, the *ScS–S* residuals can be assumed to be an index of $d\ln V_s$. If we have only thermal anomalies, $d\ln V_s$ is directly translated to the thermal anomalies, dT. The nonlinearity shown in Fig. 10 may be due to the temperature-dependent Clapeyron slope, dP/dT, or the nonlinear sensitivity of the velocity anomalies to the thermal anomalies, $\partial \ln V_s/\partial T$.

Another possibility is that we have both thermal and chemical anomalies. For example, a chemically distinct pile generated by a thermochemical plume may explain the observations (Fig. 5d). If the chemically distinct pile is a region with a larger content of impurities, the pile will have lower velocities than the surrounding regions (e.g., Tsuchiya and Tsuchiya, 2006). The center of the pile will have thicker chemically distinct regions as well as higher

temperatures, explaining the observed trend of the *ScS–S* residuals (shown in Fig. 5a). The abrupt change in the depth of the D'' discontinuity between data bins #4 and #5 may also be due to the chemical anomalies: the discontinuity at around 200 km height is inside the pile, whereas that at approximately 340 km height is outside the pile. In thermochemical plumes, we also have thermal anomalies, and the region for data bin #2 has higher temperatures than those for data bins #1 and #4. Such thermal anomalies may be responsible for the topography of the discontinuity inside the pile (e.g., Tateno et al., 2009).

References

Avants, M., Lay, T., Russell, S.A., Garnero, E.J., 2006. Shear velocity variation within the D'' region beneath the central Pacific. J. Geophys. Res. 111, B05305, doi:10.1029/2004JB003270.

Flanagan, M.P., Shearer, P.M., 1998. Global mapping of topography on transition zone velocity discontinuities by stacking SS precursors. J. Geophys. Res. 103, 2673–2692.

Garnero, E.J., Helmberger, D.V., Grand, S., 1993. Preliminary evidence for a lower mantle shear-wave velocity discontinuity beneath the central Pacific. Phys. Earth Planet. Int. 79, 335–347.

Gu, Y.J., Dziewonski, A.M., Su, W.J., Ekstrøm, G., 2001. Models of the mantle shear velocity and discontinuities in the pattern of lateral heterogeneities. J. Geophys. Res. 106, 11,169–11,199.

Hutko, A.R., Lay, T., Garnero, E.J., Revenaugh, J., 2006. Seismic detection of folded, subducted lithosphere at the core-mantle boundary. Nature 441, 333–336.

J-Array Group, 1993. The J-Array Program: system and present status. J. Geomag. Geoelectr. 45, 1265–1274.

Kanasewich, E.R., 1973. Time Sequence Analysis in Geophysics. Univ. Alberta Press, Edmonton.

Kawai, K., Sekine, S., Fuji, N., Geller, R.J., 2009. Waveform inversion for D'' structure beneath northern Asia using Hi-net tiltmeter data. Geophys. Res. Lett. 36, L20314, doi:10.1029/2009GL039651.

Kennett, B.L.N., Engdahl, E.R., 1991. Traveltimes for global earthquake location and phase identification. Geophys. J. Int. 105, 429–465.

Kito, T., Krüger, F., Negishi, H., 2004. Seismic heterogeneous structure in the lowermost mantle beneath the southwestern Pacific. J. Geophys. Res. 109, B09304, doi:10.1029/2003JB002677.

Kito, T., Rost, S., Thomas, C., Garnero, E.J., 2007. New insights into the P- and S-wave velocity structure of the D'' discontinuity beneath the Cocos plate. Geophys. J. Int. 169, 631–645.

Konishi, K., Kawai, K., Geller, R.J., Fuji, N., 2009. MORB in the lowermost mantle beneath the western Pacific: evidence from waveform inversion. Earth Planet. Sci. Lett. 278, 219–225.

Krüger, F., Weber, M., Scherbaum, F., Schlittenhardt, J., 1993. Double beam analysis of anomalies in the core-mantle boundary. Geophys. Res. Lett. 20, 1475–1478.

Lay, T., Garnero, E.J., Russell, S.A., 2004. Lateral variation of the D'' discontinuity beneath the Cocos Plate. Geophys. Res. Lett. 31, L15612, doi:10.1029/2004GL020300.

Lay, T., Hernlund, J., Garnero, E.J., Thorne, M.S., 2006. A post-perovskite lens and D'' heat flux beneath the central Pacific. Science 314, 1272–1276.

Mégnin, C., Romanowicz, B., 2000. The three-dimensional shear velocity structure of the mantle from the inversion of body, surface and higher-mode waveforms. Geophys. J. Int. 143, 709–728.

Nishida, K., Kawakatsu, H., Fukao, Y., Obara, K., 2008a. Background Love and Rayleigh waves simultaneously generated at the Pacific Ocean floors. Geophys. Res. Lett. 35, L16307, doi:10.1029/2008GL034753.

Nishida, K., Kawakatsu, H., Obara, K., 2008b. Three-dimensional crustal S wave velocity structure in Japan using microseismic data recorded by Hi-net tiltmeters. J. Geophys. Res. 113, B10302, doi:10.1029/2007JB005395.

Obara, K., Kasahara, K., Hori, S., Okada, Y., 2005. A densely distributed high-sensitivity seismograph network in Japan: Hi-net by National Research Institute for Earth Science and Disaster Prevention. Rev. Sci. Inst. 76, 021301, doi:10.1063/1.1854197.

Okada, Y., Kasahara, K., Hori, S., Obara, K., Sekiguchi, S., Fujiwara, H., Yamamoto, A., 2004. Recent progress of seismic observation networks in Japan—Hi-net, F-net, K-NET and KiK-net. Earth Planets Space 56, xv–xxviii.

Shibutani, T., Hirahara, K., Kato, M., 1995. P-wave velocity discontinuity in D'' layer beneath western Pacific with J-Array records. In: Yukutake, T. (Ed.), The Earth's Central Part: Its Structure and Dynamics. Terra Scientific Publishing Company, Tokyo, pp. 1–11.

Shearer, P.M., Masters, T.G., 1992. Global mapping of topography on the 660-km discontinuity. Nature 355, 791–795.

Shibutani, T., Tanaka, A., Kato, M., Hirahara, K., 1993. A study of P-wave velocity discontinuity in D'' Layer with J-Array records: preliminary results. J. Geomag. Geoelectr. 45, 1275–1285.

Takeuchi, N., 2007. Whole mantle SH velocity model constrained by waveform inversion based on three-dimensional Born kernels. Geophys. J. Int. 169, 1153–1163.

Tateno, S., Hirose, K., Sata, N., Ohishi, Y., 2009. Determination of post-perovskite phase transition boundary up to 4400 K and implications for thermal structure in D'' layer. Earth Planet. Sci. Lett. 277, 130–136.

Thomas, C., Garnero, E.J., Lay, T., 2004a. High-resolution imaging of lower-most mantle structure under the Cocos plate. J. Geophys. Res. 109, B08307, doi:10.1029/2004JB003013.

Thomas, C., Kendall, J.M., Lowman, J., 2004b. Lower-mantle seismic discontinuities and the thermal morphology of subducted slabs. Earth Planet. Sci. Lett. 225, 105–113.

Thomas, C., Weber, M., Wicks, W., Scherbaum, F., 1999. Small scatterers in the lower mantle observed at German broadband arrays. J. Geophys. Res. 104, 15,073–15,088.

Tonegawa, T., Nishida, K., Watanabe, T., Shiomi, K., 2009. Seismic interferometry of teleseismic S-wave coda for retrieval of body waves–An application to the Philippine Sea slab underneath the Japanese Island–. Geophys. J. Int. 178, 1574–1586.

Tonegawa, T., Hirahara, K., Shibutani, T., Iwamori, H., Kanamori, H., Shiomi, K., 2008. Water flow to the mantle transition zone inferred from a receiver function image of the Pacific slab. Earth Planet. Sci. Lett. 274, 346–354.

Tonegawa, T., Hirahara, K., Shibutani, T., Shiomi, K., 2006. Upper mantle imaging beneath the Japan Islands by Hi-net tiltmeter recordings. Earth Planets Space 58, 1007–1012.

Tono, Y., Kunugi, T., Fukao, Y., Tsuboi, S., Kanjo, K., Kasahara, K., 2005. Mapping of the 410- and 660-km discontinuities beneath the Japanese islands. J. Geophys. Res. 110, B03307, doi:10.1029/2004JB003266.

Tsuchiya, T., Tsuchiya, J., 2006. Effect of impurity on the elasticity of perovskite and postperovskite: velocity contrast across the postperovskite transition in $(Mg, Fe, Al)(Si, Al)O_3$. Geophys. Res. Lett. 33, L12S04, doi:10.1029/2006GL025706.

Yamada, A., Nakanishi, I., 1996. Detection of P-wave reflector in D'' beneath the south-western Pacific using double-array stacking. Geophys. Res. Lett. 23, 1553–1556.

Yamada, A., Nakanishi, I., 1998. Short-wavelength lateral variation of a D'' P-wave reflector beneath the southwestern Pacific. Geophys. Res. Lett. 25, 4545–4548.